Self-assembly and *in-situ* characterization of $Ti_3C_2T_x$ in Al: A step toward additive manufacturing of MXene-metal composites

*Brian C. Wyatt, Babak Anasori**

Department of Mechanical and Engineering, and Integrated Nanosystems Development Institute

(INDI), Indiana University-Purdue University, Indianapolis, 46202, USA

Highlights

- A tunable self-assembly of nanometer-thick $Ti_3C_2T_x$ MXene flakes to a micron-size Al metal powder which can be scaled for suitable for forming additive manufacturing powder beds is introduced
- Two-dimensional x-ray diffraction (XRD^2) techniques are introduced as a rational method to characterize MXene concentrations as low as 1 wt% in a bulk metal matrix
- *In-situ* hot stage XRD^2 annealing techniques are introduced as a method to characterize the effects of sintering on both materials in MXene-metal nanocomposites

Abstract

Two-dimensional (2D) transition metal carbides, known as MXenes, have grown since 2011 partly due to their impressive high electrical conductivity, stiff mechanical properties, and abundant chemically-active surface groups. These key features of MXenes make them attractive candidates for uniform coverage of metal powders for additive manufacturing of multi-functional metal composites. In this study, we report on a tunable self-assembly process of nanometer-thick 2D MXene flakes on micron-size Al particles using 1 – 10 wt% of single-to-few and multi-layer $Ti_3C_2T_x$ MXene. In addition, we discuss the characterization of these composites using 2D x-ray diffraction (XRD^2) for identification of the characteristic $Ti_3C_2T_x$ diffraction peaks. Lastly, we use *in-situ* XRD^2 paired with Vickers hardness and scanning electron microscopy/energy dispersive x-ray spectroscopy methods to understand the effect of sintering on the $Ti_3C_2T_x$ morphology and the resultant mechanical properties of the bulk composite. This study aims to assist future advances in additive manufacturing of MXene-metal composites for an array of multi-functional applications.

Keywords: MXene, metal matrix composites, additive manufacturing, *in-situ*, XRD^2, nanocomposites

This is the author's manuscript of the article published in final edited form as:

Wyatt BC, Anasori B. Self-assembly and in-situ characterization of Ti3C2Tx in Al: A step toward additive manufacturing of MXene-metal composites. Applied Materials Today. 2022;27:101451. doi:10.1016/j.apmt.2022.101451

1. *Introduction*

Two-dimensional nanomaterials are under immense demand to meet our world's need for multi-functional materials for electronic, catalytic, and structural applications since their discovery in 2004 [1]. In 2011, the family of 2D nanomaterials grew to include a large family of transition metal carbides, nitrides, and carbonitrides, which are known as MXenes.[2] MXenes are derived from their precursor via selective chemical etching in fluoride containing solutions or molten salt methods [3-7]. MXenes are represented by the chemical formula $M_{n+1}X_nT_x$, where M represents a transition metal from the 3*d* - 5*d* blocks of groups 3 - 6 of the periodic table, X is carbon or nitrogen, and T_x represents functional surface terminations, which are commonly =O, –(OH), –F, and –Cl and derived from their etching conditions [8-12]. MXenes have become a prominent nanomaterial and have found applications ranging from energy storage/catalysis, mechanical reinforcement, water purification, and CO_2 photoreduction [10, 13-22]. MXenes owe their prominence to their exceptional properties, such as metallic electrical conductivity (up to 24,000 $S \cdot cm^{-1}$) [23], high ionic mobility [24], and tunable mechanical stiffness [25-27]. Monolayer MXenes have the highest mechanical stiffness of solution processable 2D materials at 330 GPa and 386 GPa for $Ti_3C_2T_x$ and $Nb_4C_3T_x$, respectively [28, 29].

MXenes have been used in composites to improve the conductivity [30, 31], frictional properties [32, 33], and mechanical properties of a matrix material [34-38]. Recent studies have used $Ti_3C_2T_x$ MXenes as additive in metal matrices, such as Al [39, 40], Cu [32, 38], and Mg-Li [35]. While multi-layer MXenes in metal composites have shown some promise for improvement of the mechanical properties [34, 41], single-to-few-layer delaminated MXenes have shown the most promising reinforcement of the metal matrix, with a highest reinforcement of 66% on the ultimate tensile strength at only a 0.26 vol% inclusion of few-layer $Ti_3C_2T_x$ MXene in Al [40, 42].

In addition to their strengthening potential, $Ti_3C_2T_x$ MXenes' inherent stability in its hexagonal crystal structure up to 700 °C in film form and in metal matrices followed by its subsequent phase transformation to cubic TiC_y ($0.5 < y < 1.0$) above 800 °C indicates MXenes' potential to act as a unique carbide reinforcement material for both low-temperature and high-temperature melting point metals [35, 39, 41-43]. While limited data exists on the conductive properties of MXene in metal matrices [38], the improvement in the electrical conductivity in other nanomaterial-reinforced metal composites over their matrix metal illustrates potential for MXenes to act as a conductive additive to bulk metals [44-46].

Furthermore, recent advances in additive manufacturing of nanomaterial reinforced metal composites illustrates the potential of additive manufacturing for MXene-metal composites [47, 48]. As compared to other nanomaterials, MXenes' solution processability from its negative surface charge due to its plentiful surface groups lends significant potential for tunable solution-based powder mixing processes, which can potentially be scaled to industry-level powder bed batch sizes for additive manufacturing of MXene-metal composites. In addition to its solution processability, MXenes' impressive mechanical properties paired with its oxygen-containing surface groups, which lend sites for primary bonding between the metal matrix and MXene flakes as seen previously through an intermediary Al_2O_3 phase between $Ti_3C_2T_x$ in an Al matrix [40], lend potential for MXene to act as a stiff reinforcement material with strong bonding potential to the matrix metal.

While MXene has significant potential in additive manufactured metal composites, this research is currently limited by two factors: i) uniform dispersion of single-to-few layers of MXene flakes in the matrices [34, 35, 38, 39], and ii) the detection of MXenes and their morphology in metal matrices. A common method for identification and characterization of MXenes is through

x-ray diffraction (XRD) [2, 25]. Although electron microscopy methods reveal local morphology, XRD may be more beneficial toward bulk additive processing of MXene-metal composites as XRD analyzes a larger area than local electron microscopy. In MXene literature, XRD analysis has identified the characteristic diffraction patterns of MXene as the out-of-plane (00ℓ) and in-plane (010) and (110) peaks [49]. However, XRD of MXene in metal matrices is currently limited as XRD can either detect multi-layer non-delaminated MXene [39], high MXene concentrations (>10 wt%) [35], or recovered MXene after metal dissolution with acids [35]. To date, no studies have extensively used XRD to characterize delaminated single-to-few layer MXene within metals or to understand the effects of sintering on MXene morphology within the metal matrix. This bottleneck limits identification of the effects of additive manufacturing processes on the integrity of MXene flakes in metals.

The combination of the promise of a solution-based mixing process for MXene-metal additive manufacturing combined with need for detection and analysis of the morphologies of MXene in low concentrations via XRD led to this study. In this paper, we establish a tunable self-assembly solution-based mixing process of single-to-few layer $Ti_3C_2T_x$ between 1 to 10 wt% and multi-layer stacks of 5 wt% $Ti_3C_2T_x$ in an Al powder matrix. In addition, we utilize 2D XRD (XRD^2) to characterize bulk samples of $Ti_3C_2T_x$-Al and evaluate the condition and morphology of $Ti_3C_2T_x$ in Al via characteristic $Ti_3C_2T_x$ XRD patterns. After establishing $Ti_3C_2T_x$ in the metal matrix, we then use *in-situ* hot-stage XRD^2 analysis to characterize the annealing process of the $Ti_3C_2T_x$-Al composite and use this analysis to understand the thermal, mechanical, and morphological behavior of $Ti_3C_2T_x$ in the Al matrix during annealing. The combination of our tunable self-assembly followed by in-depth XRD^2 characterization lays groundwork for future studies on MXene-metal nanocomposites produced via additive manufacturing.

2. *Materials & Methods*

2.1 $Ti_3C_2T_x$ Synthesis

The $Ti_3C_2T_x$ used in this paper is synthesized from 4 g of its precursor MAX phase Ti_3AlC_2 through selective etching of Al via an acidic mixture is prepared by using 12 mL of 48% HF solution (Sigma-Aldrich), 72 mL of 37% HCl solution (Sigma-Aldrich), and 36 mL of de-ionized H_2O. The acidic mixture is placed into a high-density polyethylene (HDPE) container with a magnetic Teflon-coated stir bar placed in an oil bath on a Corning 6795-620D Digital Stirring Hot Plate. The Ti_3AlC_2 is then slowly placed into the acid over a 3 min period, then mixed at 300 RPM at 35 °C for 24 h. After this period, the exfoliated $Ti_3C_2T_x$ in an acidic solution is repeatedly washed with DI water via centrifugation in a 175 mL Falcon® Conical Centrifuge Tube in an Eppendorf centrifuge with a S-4-72 rotor at 2380 RPM for 5 min until the supernatant reaches a pH of 6. After acid washing, the $Ti_3C_2T_x$ is delaminated using 4 g of anhydrous LiCl (Sigma-Aldrich) in 200 mL of DI water in a HDPE container with a Teflon-coated stir bar in an oil bath for 1 h at 1000 RPM at a temperature of 65 °C under constant Ar flow. After delamination, the solution is washed three times at 14,000 RPM in 50 mL Fisher Scientific centrifuge tube in a Thermo-Fisher ST16 Centrifuge using a Fiberlite F15-8x50cy rotor for 5 minutes, 10 min, and 20 min for the first, second, and third washes, respectively. After this step, the dispersed $Ti_3C_2T_x$ solution is centrifuged at 2,380 RPM for 30 min, where the supernatant of this cycle is used as the delaminated, large-flake $Ti_3C_2T_x$ solution. Multi-layer (clay) $Ti_3C_2T_x$ was achieved through use of the clay-like sediment of this last 2,380 RCF for 30-minute cycle. The concentration of the supernatant is determined by vacuum-assisted filtration of 10 mL of solution, overnight drying in a vacuum oven at 60 °C, then weighing of the final free-standing $Ti_3C_2T_x$ film.

To test the quality of the $Ti_3C_2T_x$ batches used in our composites, we tested this film using a four-point probe setup using a Keithley 2400 SMU. We spaced these probe tips in a measured 1 cm by 1 cm square on the surface of the $Ti_3C_2T_x$ film to measure the resistance of the surface. After measuring the resistance, we measured the thickness of the film using a Holite digital micrometer (Part No. 4354523152). The thickness of the films was normally in the range of 50 μm thick. We calculated the conductivity of these films using the resistance and film thickness, which was typically >10,000 S/cm.

The zeta measurements for $Ti_3C_2T_x$ were conducted using a Malvern Zetasizer Nano Series using a fresh Malvern DTS1070 folded capillary zeta cell. The $Ti_3C_2T_x$ was diluted in water to 0.1 $mg \cdot mL^{-1}$ and then shaken before the addition of 0.5 mL of the $Ti_3C_2T_x$ water solution to the capillary zeta cell. The cell was then inserted into the Zetasizer Nano to measure in 3 cycles of 15 measurements with a 60 second delay between each cycle.

2.2 Al Flake Powder Preparation

Al flakes with freshly exposed non-oxidized Al layers were prepared by placing 5 g of Al spherical powder (APS 3.0-4.5 µm, Thermo Scientific, Catalog No. AA4100018) in 125 mL of 200 proof ethanol (Decon Labs, CAS 64-17-5,7732-18-5) into HDPE container for a final Al concentration of 40 mg mL^{-1}. Yttria-stabilized zirconia balls (10 mm) were added to the mixture at a ball-to-powder ratio by mass of 40:1. The entire assembled container was sealed with 99.9% Ar for 10 minutes by bubbling Ar into the Al in ethanol solution followed by sealing the lid with Parafilm (Parafilm M Bemis Catalog No. P6543). The assembled container is then placed in a rotating jar ball mill at an incline of 45° with respect to the axial direction and rotated at 64 RPM in a Shimpo PTA-02 Jar Mill for 24 h. Alternate BPR and milling times were completed similarly,

with the only differences in the total mass of the Yttria-stabilized zirconia balls and the milling times, respectively.

The zeta measurements for Al were conducted after ball milling using a Malvern Zetasizer Nano Series using a fresh Malvern DTS1070 folded capillary zeta cell. 1 mL of ethanol containing 40 mg of Al was added to 10 mL glass vials, then the corresponding vol% water was added to each glass vial to gain a range of water vol% from 40 vol% to 80 vol%. Each vial was then shaken before the addition of 0.5 mL of the Al water-ethanol solution to the capillary zeta cell. Between each solution, the interior of the capillary zeta cell was thoroughly washed with a 70 vol% ethanol spray bottle (~50 mL) and emptied before the addition of the next Al water-ethanol solution. The cell was then entered in the Zetasizer Nano to measure in 3 cycles of 15 measurements with a 60 second delay between each cycle.

2.3 Preparation and Treatment of $Ti_3C_2T_x$ MXene – Al Powder

To prepare the $Ti_3C_2T_x$-aluminum mixture, 1 g of the dispersed ball milled Al in ethanol solution is added to a glass flask with a Teflon-coated magnetic stir bar on a stir plate. After adding aluminum, DI water is then added to the flask just below the corresponding to the vol% of water necessary in the water-ethanol solution(with accounting to the water in the to-be-added $Ti_3C_2T_x$-water solution). After mixing for two minutes, the 2 wt% of $Ti_3C_2T_x$ is added from its water-based solution to raise the overall water-ethanol concentration to 60 vol% de-ionized water (the 70 vol% sample was similarly completed to 70 vol% water addition). Our $Ti_3C_2T_x$ solutions were typically ~5 mg/mL in concentration, so we added ~34 mL pure DI water to the Al ethanol solution before adding ~4 mL of our $Ti_3C_2T_x$ solution to achieve 2 wt% $Ti_3C_2T_x$ in Al in a water-ethanol solution at 60 vol% concentration of water. The solution is then mixed at 1000 RPM for 10 minutes at room

temperature until a separation of MXene-Al precipitate slurry and clear solution is seen. The stirring is then stopped, and the solution is then left to settle.

The clear solution is then removed via pipetting and the remaining slurry is filtered via vacuum-assisted filtration with 2.5 μm pore diameter filter paper (Whatman). For non-clear solution (fully adsorbed) batches of $Ti_3C_2T_x$, the solution was left for 2 minutes and was then filtered without pipette-based removal of the solution. The control Al samples were similarly processed, without pipette-based removal of the solution. During filtration, the filtered powder is thoroughly washed by a spray bottle filled with 200 proof ethanol to remove any remaining water. After filtration of each mixed powder, the damp powder is dried >100 °C in a vacuum oven overnight. The larger batch of $Ti_3C_2T_x$-Al mixture was completed similarly to the 1 g batch, with the addition of 4 g Al total to the glass flask followed by the addition of 2 wt% $Ti_3C_2T_x$. The clear solution was removed via pipette and then filtered and dried according to the previously established methods.

2.4 Characterization of $Ti_3C_2T_x$ – Al Powder

Dispersion of $Ti_3C_2T_x$ within the Al powder is analyzed via field-emission scanning electron microscopy (FESEM) using a JEOL JSM-7800f FESEM with a lower electron detector at an acceleration voltage of 5 kV. EDS point scans were conducted by increasing the acceleration voltage to 15 kV and zooming the scope in to 1,000,000x magnification and taking a 30s exposure scan with an EDAX octane super detector, which was subsequently analyzed for atomic composition using the EDAX TEAM software. All powder samples were coated with Au via sputtering to improve the conduction path of electrons for sharper images. The presence of $Ti_3C_2T_x$ is determined by the differences in the flake morphology, where determination $Ti_3C_2T_x$ is concluded by the existence of “folds” in the flake arrangement. The average lateral dimension of

the $Ti_3C_2T_x$ flakes and Al flakes was calculated using ImageJ software. The composition is further analyzed using a Bruker D8 x-ray diffractometer with Cu Kα (λ = 1.5406 Å) emitter with a VANTEC 500 detector. The focused scans were conducted via centered scans at 10° and 60° 2θ using a still emitter/detector method for 15 minutes total. The long exposure still scan at 10° 2θ was similarly completed using a 60-minute total scan time. The full spectrum was captured using a paired emitter/detector movement program in a stepwise method with steps centered at 5° to 75° 2θ in increments of 5° 2θ for each step with a timestep of 60 s per step. The corresponding XRD[2] data is analyzed via merged detector images as well as a full-spectrum integration scheme in the DIFFRAC.SUITE EVA software to calculate traditional XRD plots. Traditional 0D XRD scans were conducted using a Lynxeye XE detector with a step size of 0.02° 2θ with a dwell time of 24 seconds per step from 59° to 64° 2θ and was analyzed using the DIFFRAC.SUITE EVA software.

Differential scanning calorimetry scans were conducted by placing 100 mg of vacuum-dried Al or mixed $Ti_3C_2T_x$-Al powders of various $Ti_3C_2T_x$ concentrations into a clean Al_2O_3 pan with lid in a TA Q600 simultaneous thermal analyzer under continuous scanning mode while ramping 3.5 °C/min up to 800 °C.

2.5 Characterization of pressed $Ti_3C_2T_x$-Al billets

Once dry, 300 mg of the $Ti_3C_2T_x$-Al powder was added to a boron nitride (BN) spray-coated (ZYP Boron Nitride Mold Primer, Model No. 3-1047-00-30) 13 mm diameter $Cr_{12}MoV$ hardened steel die (Columbia International, Model No. CIT-LPD-SC13). The mixed powder was then compressed in the steel die at room temperature at 300 MPa for 5 min using a Carver 3889 Hydraulic Hot Press in ambient conditions. Once 5 min had passed, the billet was then removed from the mold. After pressing, the remaining boron nitride on the surface of the $Ti_3C_2T_x$-Al pressed billet was removed through the use of 300 grit SiC sandpaper and was sanded until the exterior

surface was removed. After BN removal, the density of the billet was measured using an Archimedes water immersion approach. After testing using this method, all billets were dried in the vacuum oven overnight at 100 °C. Densification was calculated using an ideal density evaluated using the rule-of-mixtures approach with 4.2 g/cm^3 and 2.7 g/cm^3 for $Ti_3C_2T_x$ and Al, respectively.

For *in-situ* XRD[2] characterizations, the $Ti_3C_2T_x$-Al billets were once-again sanded with 300 grit SiC sandpaper to remove any traces of oxides on the surface from the Archimedes density testing before they were affixed to an AlN substrate using stainless steel pins at the edges of the billets within an Anton-Parr DHS 1100 domed hot stage. After affixing the sample on the substrate, a protective graphite dome was placed over the samples and left in an ambient environment. The test on the (311) peak of Al was conducted by focusing the scan at 75° 2θ and scanning for 60 s per step. The test for the (311) peak of Al was started at room temperature (taken as 40 °C, as the actual room temperature in this lab fluctuated around 28-31 °C) before ramping up to 550 °C at a ramp rate of 60 °C/min and taking scans once 550 °C was reached (taken as 0 min), 30 minutes after 550 °C was reached (taken as 30 min), and after 1 h 550 °C was reached (taken as 60 min) before rapid cooling using forced air convection over the surface of the protective graphite dome. After 40 °C was reached again, another scan was taken before removing the billet from the hot stage apparatus. A similar experimental setup was taken to analyze the (00ℓ) peaks of 10 wt% single-to-few flake and multi-layer flakes of $Ti_3C_2T_x$ in Al, but the scan was focused at 5° 2θ for 60 s/step while the temperature was ramped up at a rate of 60 °C/min to 100 °C, 200 °C, 300 °C, 400 °C, 500 °C, and 550 °C with a scan taken at each of these temperature points before ramping to the next temperature. After 550 °C was reached, the stage was once again cooled to 40 °C at a roughly averaged 30 – 40 °C/min before another scan was taken. CTE is calculated by derivation

of the *a*-LP (*a*) from the Al (311) peak assuming cubic structure and is derived by the equation CTE = $((a_f-a_o)/a_o)/(\Delta T)$. After removal from the hot stage setup, the density of the billet was again measured using an Archimedes water immersion approach.

After the *in-situ* hot stage annealing tests were conducted, the billets were then removed and sanded slowly up to 1800 grit sandpaper to make a fairly smooth surface for Vickers hardness testing. Vickers hardness testing was conducted using a Phase II Micro Vickers Hardness Tester (Model No: 900-390) equipped with a pyramidal indenter using a 0.5 kg (4.9 N) indentation force with a dwell time of 15 s. To take repetitive tests, the indenter was moved at least 2 mm away from the previous test before the next indentation was taken. The Vickers hardness was calculated using an average of the two distances between opposite corners in the square pyramidal indentation.

After Vickers hardness testing, the non-annealed and annealed 5 wt% ML $Ti_3C_2T_x$ samples were prepared for fracture cross-section SEM/EDS analysis through physically breaking the billet with pliers before they were mounted onto the side of a SEM stage using double-sided amorphous carbon tape for analysis. To ensure the EDS data was not affected by this SEM stage, the exposed fractured cross-section was raised approximately 1 mm above the stage before securement. SEM backscatter images were taken at a working distance of 12 mm from electron probe with an acceleration voltage of 15 kV. EDS point scans were conducted through similar methods as the powder $Ti_3C_2T_x$-Al powder mixture.

3. *Results and Discussion*

In order to begin our self-assembly process of $Ti_3C_2T_x$ MXene to the Al matrix, we first start with the synthesis of $Ti_3C_2T_x$ and is described fully in the methods section [43]. The etching method of $Ti_3C_2T_x$ from its Ti_3AlC_2 MAX phase precursor and MXene's final dispersion in water

is shown schematically in Figure 1a. Due to MXenes' surface groups, MXenes have a negative surface charge in water or polar organic solvents, such as ethanol [50]. In order to characterize this surface charge of $Ti_3C_2T_x$ in water, we measured the zeta potential of the $Ti_3C_2T_x$ dispersion, which was -35.7 ± 9.5 mV in DI water (Figure 1b) in agreeance with previous studies [51].

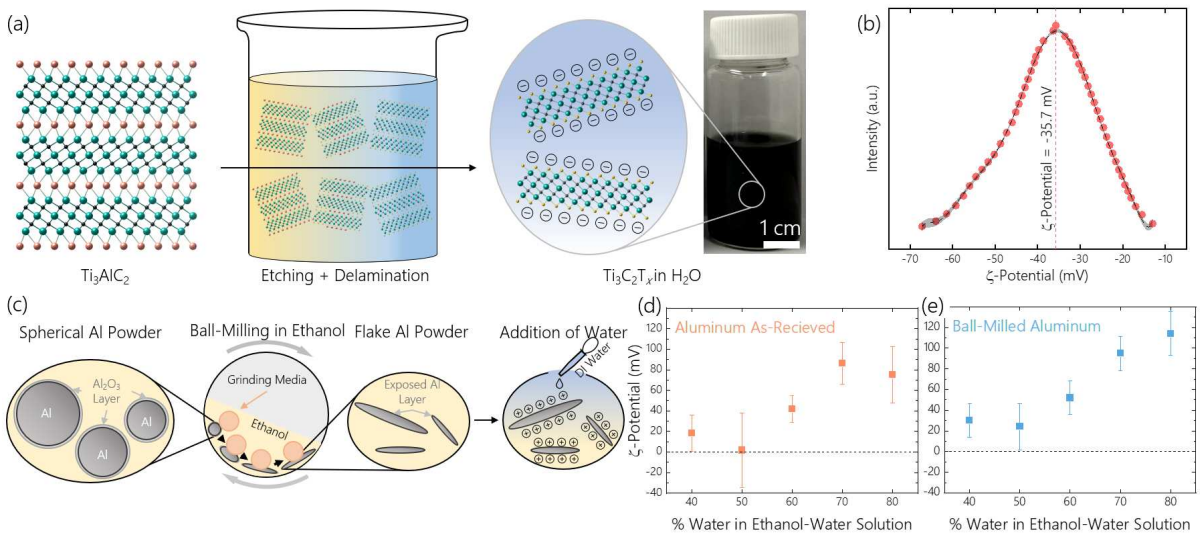

Figure 1. Preparation and characterization of $Ti_3C_2T_x$ and Al for electrostatic self-assembly. (a) Schematic of selective etching and delamination of $Ti_3C_2T_x$ from Ti_3AlC_2 result in surface terminated $Ti_3C_2T_x$ flakes, which appear black in solution. (b) Zeta potential of $Ti_3C_2T_x$ MXene black solution in (a) showing surfaces of these flakes are negatively charged, with an average zeta potential of -35.7 ± 9.5 mV. (c) The schematic of ball-milling illustrates the exposure of a non-oxidized Al surface by ball milling spherical 3.0-4.5 µm Al powder in a pure ethanol solution. The addition of water can ionize the surface of the Al forming Al^{3+}. Zeta potential of as-received Al powder (d) and ball-milled Al after 24 h with a BPR of 40:1 (e) from a 40-80 vol% water concentration of an ethanol-water solution. The zeta potential of Al in an ethanol-water solution increases when the Al is ball milled in ethanol due to the exposed Al surface.

After synthesis of $Ti_3C_2T_x$, we focus on preparation of Al powders for electrostatic self-assembly (details in Methods). Since the surface of $Ti_3C_2T_x$ is negatively charged, our electrostatic self-assembly process requires the surface of Al to have a positive charge. To do so, it is necessary to alter the surface of Al to an Al^{3+} oxidation state [52]. Al is ionized in the presence of water, however, the rate is slowed by the 3-4 nm thick native Al_2O_3 layer on the surface [53, 54]. The magnitude of the surface charge of Al can be increased by exposing non-oxidized Al surfaces

before the introduction of water [53]. We used rolling jar ball milling (Figure 1c) to expose fresh surfaces of Al in an ethanol solution where ethanol maintains the fresh Al surfaces [53]. We identified that 24 h ball milling at a ball to powder ration (BPR) of 40:1 is best to deform Al spheres to Al flakes with fresh surface (Figure S1). This process converted spherical Al powder with a diameter of 2.04 ± 1.85 μm into Al flakes with an average of 6.57 ± 6.54 μm diameter (Figure S1) which increased the surface area of Al at an average of 300%. Next, we explored the effect of different concentrations of water solution on the zeta potential of the dispersed Al in the ethanol-water solution (Figure 1d and e). We found that the positive surface charge of Al increased in both types of Al (as received and ball milled) as the water concentration is increased from 40 vol% to 80 vol%. However, the ball-milled Al flakes illustrate an averaged ~25% increase in zeta potential as compared to the as-received Al powder. Although the surface charge of Al continually increased with an increased concentration of water, a 100 vol% concentration solution of water results in formation of Al_2O_3 particles on the surface of Al as indicated by scanning electron microscopy (SEM) and energy dispersive spectroscopy (EDS) (Figure S2 & Tables S1 and S2). Therefore, we used a mixture of water and ethanol to promote electrostatic adsorption of $Ti_3C_2T_x$ to ball milled Al and mitigate the oxidative effects of water during mixture.

After we investigated the effects of DI water addition on the surface charge and oxidation of our ball milled Al, we focused on the electrostatic self-assembly of ball-milled Al with $Ti_3C_2T_x$. We used a 60 vol% concentration of water due to the i) relatively high positive zeta potential of the ball-milled Al (52.0 ± 16.2 mV) which we hypothesized would result in single-to-few layer self-assembly of $Ti_3C_2T_x$ (– 35.7 ± 9.5 mV) by mutual self-adsorption-based neutralization of surface charges and ii) slow oxidation of Al as compared to mixture in pure water. To make the self-assembled $Ti_3C_2T_x$-Al powder, we first added the milled Al flakes in pure ethanol to a glass

container (Figure 2a) and then added water to a concentration of 60 vol% water. To fully cover the surface of our Al flake size, we calculated a necessary weight fraction of $Ti_3C_2T_x$ in Al at 2.03 wt% using 1 nm as the thickness for $Ti_3C_2T_x$, [28] 150 nm average thickness and 6.6 µm diameter of Al flakes, and 4.2 g/cm^3 and 2.7 g/cm^3 for the densities of $Ti_3C_2T_x$ and Al, respectively. We tested this weight fraction experimentally through the addition of $Ti_3C_2T_x$ (Figure 2b) drop-wise into Al solution while mixing (Figure 2c). In this experiment, ~2 wt% of $Ti_3C_2T_x$ flakes resulted in a near-clear solution (Figure 2d). The sedimentation of $Ti_3C_2T_x$-Al suggests cancellation of the surface charges between $Ti_3C_2T_x$ and Al, resulting in an unstable $Ti_3C_2T_x$-Al particle, which causes separation from the solution.

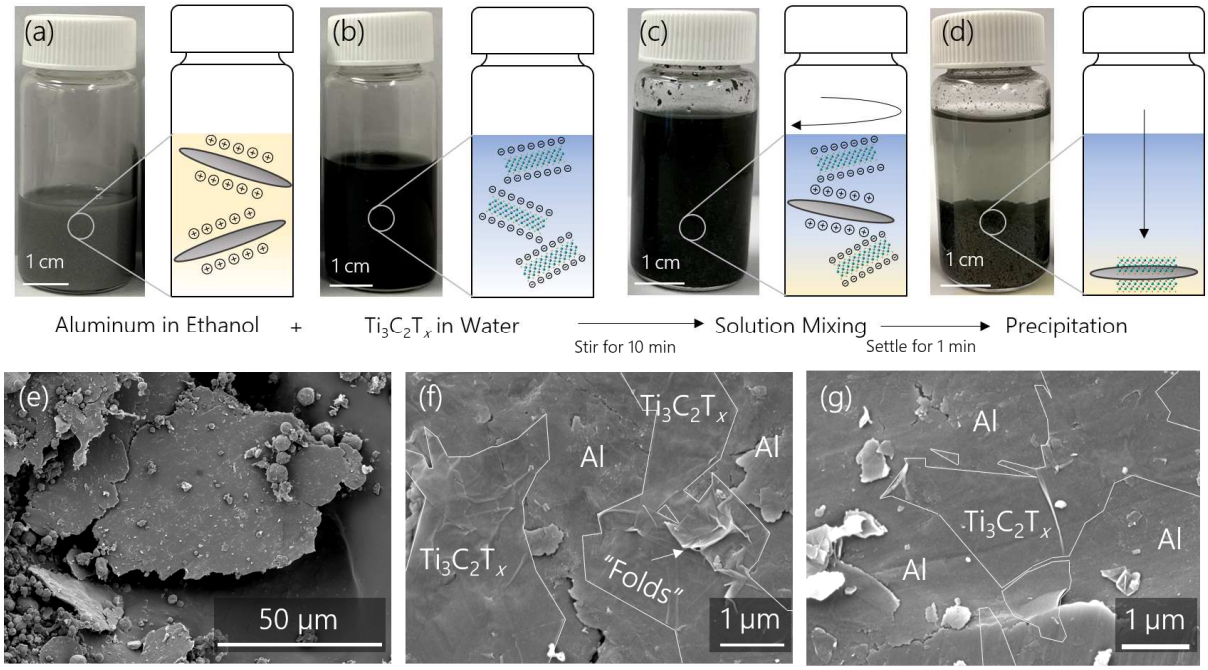

Figure 2. Solution mixing process and self-assembly of Al flakes and $Ti_3C_2T_x$ MXene solution. (a) Ball milled Al flakes in an ethanol solution (b) single-to-few-flake dispersion of $Ti_3C_2T_x$ MXene in de-ionized water, (c) Mixture of Al and $Ti_3C_2T_x$ in a 60 vol% water and 40 vol% ethanol solution. (d) complete separation of 2wt.% $Ti_3C_2T_x$-Al self-assembly from the ethanol-water solution after settling for 1 minute. (e, f, g) SEM images of $Ti_3C_2T_x$-Al self-assembled powder show near complete coverage of the Al flakes by $Ti_3C_2T_x$ (e), with two higher magnification SEM images (f-g), which illustrates the single-to-few layer $Ti_3C_2T_x$ coverage of Al's surface. The

$Ti_3C_2T_x$ flake coverage suggests that the adhesion of negatively charged $Ti_3C_2T_x$ can cancel positively charged Al with a similar charge magnitude.

The destabilization of negatively charged $Ti_3C_2T_x$ and positively ball-milled Al at 2 wt% in solution suggests near-complete coverage of the Al with single-to-few layer flake $Ti_3C_2T_x$. Since our method is nm-on-µm self-assembly, which means nanometer-thick $Ti_3C_2T_x$ MXene flakes are self-assembled on ball-milled Al powder with µm lateral sizes and submicrometer thicknesses, SEM images can be used to identify the MXenes flakes on Al particles as evidenced by Figure 3e-g. We marked the edges of the MXene flakes with solid white lines in Figure 2f-g. The identified morphological characteristics of single-to-few layer $Ti_3C_2T_x$ on Al is established in Figure S3. The average flake size distribution of 2 wt% $Ti_3C_2T_x$ onto Al is shown in Figure S4. We also evaluated the non-destabilized weight fractions of $Ti_3C_2T_x$ with Al at fractions lower or higher than 2 wt% $Ti_3C_2T_x$ (Figure S5). We noticed in our mixing that less than 2 wt% $Ti_3C_2T_x$ flakes resulted in a grey solution after mixing, which is evident of still-dispersed Al, and only results in partial coverage (Figure S6a-c). More than 2 wt% $Ti_3C_2T_x$ flakes resulted in a dark green/black solution, which is evident of still-dispersed $Ti_3C_2T_x$ flakes. One method to increase the MXene content with self-assembly is to increase the water concentration in the solution from 60 vol% to 70 vol%. This increases the surface charge of the Al from 52 ± 16.2 mV to 95 ± 16.6 mV (Figure 1e), which permits higher content assembly of $Ti_3C_2T_x$ (5 wt%) to Al before destabilization (Figure S6d-f), but makes mitigation of oxidation more difficult (Figure S2b). We also noticed that mixing times (Figure S7) and stir rate (Figure S8) affected the $Ti_3C_2T_x$ dispersion. In addition, our electrostatic adsorption process proved to be scalable for applications requiring a larger amount of a $Ti_3C_2T_x$-Al powder mixture (Figure S9). The scalability and tunability of our electrostatic adsorption process suggest this process is feasible for additive manufacturing toward the formation of bulk $Ti_3C_2T_x$-Al metal nanocomposites.

Afterwards, we focused on the identification of $Ti_3C_2T_x$ in a bulk Al sample. We formed a solid sample as described in the Methods section. Our room-temperature compaction approach reached around 84 ± 2% densification amongst Al and 1, 2, and 5 wt% $Ti_3C_2T_x$-Al powders. Afterwards, we conducted XRD to identify $Ti_3C_2T_x$ in the bulk sample. We first utilized traditional zero-dimensional point (0D) powder XRD, which did not detect $Ti_3C_2T_x$ at or lower than 2 wt% even at long scan times (Figure S10). We speculated this was due to the low diffraction signal of $Ti_3C_2T_x$ at low weight fractions (< 2 wt%). Previous studies have identified that traditional 0D XRD captures a limited amount of the available diffraction signal [55]. The use of 2D XRD (XRD^2) improves the ability to capture a larger portion of this diffraction signal [56], which we hypothesized would improve our odds of capturing low diffraction signal of $Ti_3C_2T_x$ in bulk Al. Therefore, we focused on the use of XRD^2 to detect small amount of $Ti_3C_2T_x$ (≤ 2 wt%) in bulk Al.

With the use of XRD^2, we focused on the detection of standard $Ti_3C_2T_x$ peaks. The (002) peak, if present, would appear between 5-9° 2θ based on the flakes interlayer distance and the (110) peaks of $Ti_3C_2T_x$ at 2θ ~ 61° [3, 25, 49]. In addition, XRD^2 scans can identify any crystalline Al_2O_3 possibly formed during the process. Figure 3 illustrates the raw XRD^2 scans and full spectra scans for Al and Al reinforced by 1, 2, 5, and 10 wt% single-to-few layer and 5 wt% multi-layer flakes of $Ti_3C_2T_x$ in a solid billet compressed at room temperature. Figure 3a-f show a focused 10° 2θ still XRD^2 scan for all the samples and Figures 3g-l illustrate the full spectra scans. The grey lines running through all full spectra scans represent standard (111), (200), and (220) peaks of Al from left to right, respectively. The spectra of the 10° 2θ and 60° 2θ focused scans for each sample are shown as the leftmost and rightmost insets, respectively, in Figure 3g-3l. Finally, Figure 3m-r

illustrates a focused 60° 2θ still XRD[2] scan for Al and Al reinforced by 1, 2, 5, and 10 wt% single-to-few layer and 5 wt% multi-layer flakes of $Ti_3C_2T_x$, respectively.

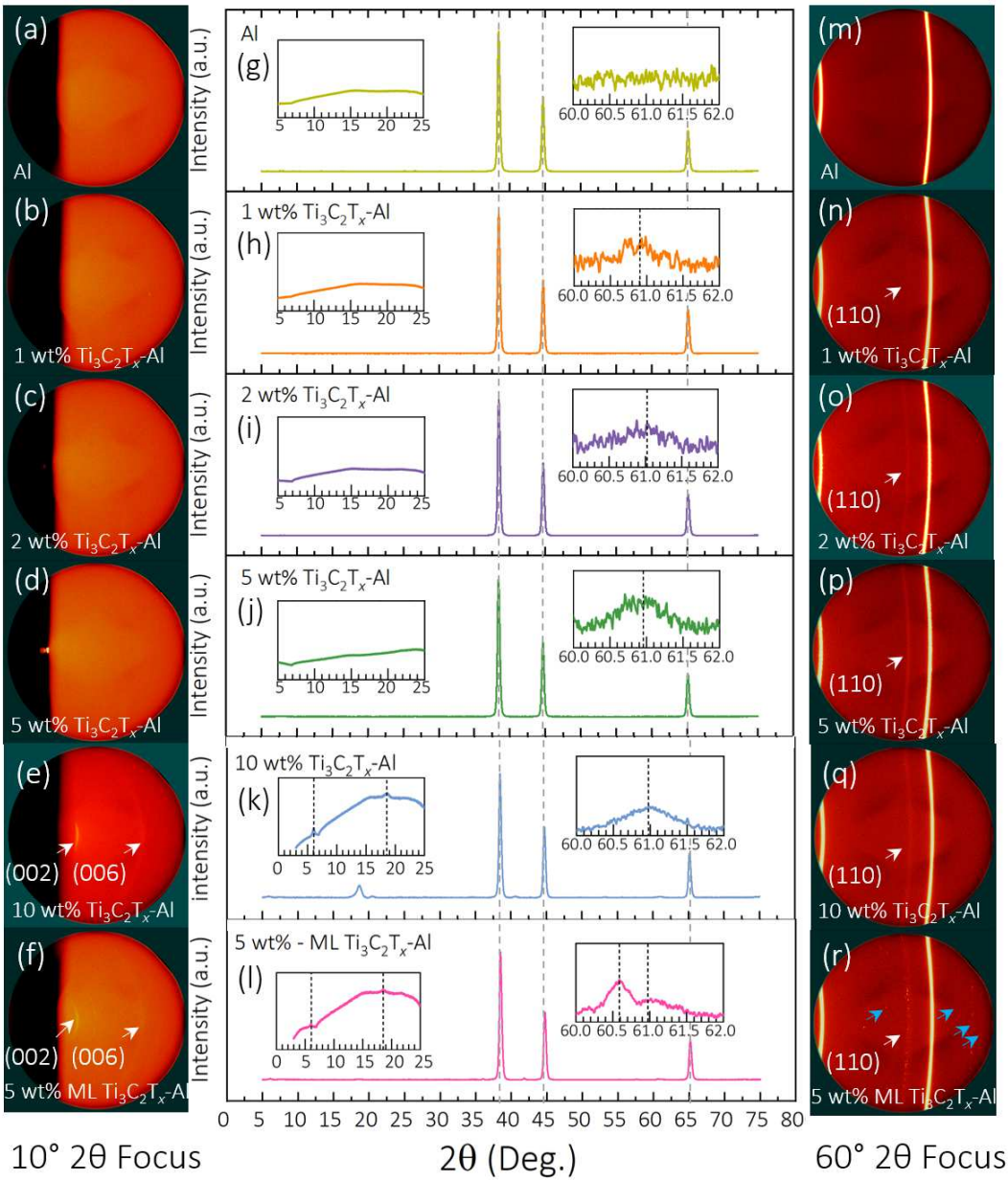

Figure 3. XRD[2] of Al and Al reinforced by 1, 2, 5, and 10 wt% single-to-few layer and 5 wt% multi-layer flakes of $Ti_3C_2T_x$ in a solid billet compressed at room temperature. (a-f) 10° 2θ still focus with exposure times of 15 minutes for all the samples. The spectra captured is 0° (leftmost side) to ~25° (rightmost side). (g-l) Full spectra (5° to 75° 2θ) captured using a XRD[2] detector. Leftmost inset is the 10° 2θ still focus and rightmost inset is a small portion of the 60° 2θ still focus for all the samples. The dotted grey line throughout all full spectra images represents primary

Al (111), (200), and (220) peaks. The rightmost inset in (h-l) of the $Ti_3C_2T_x$-Al bulk samples have a dotted black line, which represents the center of the (110) peaks of $Ti_3C_2T_x$ in the sample while the leftmost inset in (k-l) have a dotted black line which represent the (002) and (006) peaks of $Ti_3C_2T_x$. (m-r) 60° 2θ still focus with exposure times of 15 minutes for all the samples. The spectra captured is ~45° (leftmost side) to ~75° (rightmost side).

To confirm the presence of $Ti_3C_2T_x$ in these metal matrix composite billets, we analyzed our XRD^2 data to identify the in-plane (110) and out-of-plane (00ℓ) diffractions of $Ti_3C_2T_x$. The analysis of the data around 61°, where the $Ti_3C_2T_x$ (110) peak is expected, indicated the presence of $Ti_3C_2T_x$ in 1, 2, 5, and 10 wt% $Ti_3C_2T_x$ composites as shown in the right insets in Figure 3g-l. The raw XRD^2 scans illustrate these (110) peaks faintly which is pointed by an arrow in Figure 3m-r. The identification of this peak in the $Ti_3C_2T_x$-containing samples, which is not seen in the pure Al samples, confirm the presence of $Ti_3C_2T_x$ in our $Ti_3C_2T_x$-Al bulk samples. The increase in intensity of (110) ~61° 2θ peak with increasing the concentration of $Ti_3C_2T_x$ confirms this peak is due to the increased concentration of $Ti_3C_2T_x$. To further confirm our method does not lead to significant crystalline oxide formation (Al_2O_3) due to water-based mixing and examine the detection of Al_2O_3 formation, we mixed the $Ti_3C_2T_x$-Al in water-ethanol solution for longer time (30 minutes) to increase the chance of Al oxidation. The XRD^2 results (Figure S11) showed peaks of small crystalline Al_2O_3 using XRD^2. As none of the Al_2O_3 peaks are seen in our mixed composites samples (Figure 3), it is fair to conclude that our mixing method does not lead to detectable Al_2O_3 formation due to the water-based mixing.

The (00ℓ) peaks of $Ti_3C_2T_x$ in the bulk $Ti_3C_2T_x$-Al were not detectable in our 10° 2θ focus (0° to 25°) scans at 15 min acquisition times up to a 5 wt% inclusion of single-to-few layer $Ti_3C_2T_x$ (Figure 3a-d). To ensure that this was a feature of the sample and not scan time, we further increased our scan times for 1 – 5 wt% inclusions of $Ti_3C_2T_x$ in Al at 10° 2θ from 15 min to 1 hour. However, we were still unable to detect the (00ℓ) peaks in our single-to-few layer 1, 2, and

5 wt% $Ti_3C_2T_x$-Al bulk samples (Figure S12). An explanation for phenomena could potentially be that the (00ℓ) peaks of $Ti_3C_2T_x$ are of the basal plane, which is based on out-of-plane lattice parameters and requires ordered stacking of $Ti_3C_2T_x$ layers [57]. Although in most $Ti_3C_2T_x$ films the MXene has been fully delaminated, these (00ℓ) peaks are commonly seen in diffraction patterns because of regularly stacked flakes in free-standing films [58]. As evidenced by our SEM images shown in Figure 2e-g, our dispersions of $Ti_3C_2T_x$ are mostly single-to-few layer flakes with no clear stacking order. Based on our geometry calculations 5 wt% single-to-few layer $Ti_3C_2T_x$ creates almost 3-4 layer stacked $Ti_3C_2T_x$ coverage of Al particle. It was shown recently that stacking three layers of $Ti_3C_2T_x$ films on a glass slide results in a detectable the (002) peak [59]. In another study about 20-nm-thick $Ti_3C_2T_x$ MXene film was necessary to detect the (002) peak [60]. However, in dealing with few-layer stacking of MXene, the out-of-plane peaks are highly dependent on number of MXene flakes and alignment of the basal planes. In both these studies, MXene films were regularly stacked and the XRD patterns were analyzed in the presence of no other material. We hypothesize that the lack of (00ℓ) peaks in our 5 wt% sample is likely due to limited number of stacked $Ti_3C_2T_x$ flakes (<3 layers of $Ti_3C_2T_x$ [59]), disordered stacking at the Al grain boundaries, and the presence of Al as the main material component (95 wt%). To test this, we prepared higher concentration of $Ti_3C_2T_x$ (10 wt%) as well as partially delaminated 5 wt% multi-layer (5 wt% ML) clay $Ti_3C_2T_x$.

In the XRD[2] scans of 10 wt% $Ti_3C_2T_x$-Al and 5 wt% ML $Ti_3C_2T_x$-Al billets, we identified the (002) and (006) peaks of $Ti_3C_2T_x$ (Figure 3e-f, k-l). The appearance of $Ti_3C_2T_x$ (002) peak in 10 wt% $Ti_3C_2T_x$ indicate that the increase in MXene content leads to enough flake restacking to detect the (00ℓ) peaks inside an Al matrix. SEM images (Figure S13 a-d) reveal the differences in flake morphology between 5 and 10 wt% single-to-few layer $Ti_3C_2T_x$. In both samples restacking

of $Ti_3C_2T_x$ flakes occurs because $Ti_3C_2T_x$ contents are higher than the needed single-flake-coverage as we calculated before (2.03 wt%). However, the restacked flakes in the single-to-few layer 5 wt% $Ti_3C_2T_x$ in Al are likely less layered (<3 layers of $Ti_3C_2T_x$ [59]) and less uniform as compared to the 10 wt% $Ti_3C_2T_x$ in Al. The XRD^2 results of the multi-layer clay 5 wt% ML $Ti_3C_2T_x$-Al sheds light on the effect of stacked particles, in which the (002) and (006) are clearly detected (Figure 3f, k). The detection of the (00ℓ) peaks only in multi-layer 5 wt% $Ti_3C_2T_x$ and 10 wt% $Ti_3C_2T_x$ in Al indicates that (00ℓ) peaks appears only when MXene formed ordered stacking of individual flakes [43]. In addition, the small signal "dots" on the (110) $Ti_3C_2T_x$ pattern in the 60° 2θ focus of 5 wt% ML $Ti_3C_2T_x$-Al sample (Figure 5e) likely is due to stacked layers of $Ti_3C_2T_x$ in the particles of ML $Ti_3C_2T_x$ (Figure S14) [43]. The crystalline particles are shown in XRD^2 scans which correspond to $Ti_3C_2T_x$ diffraction signal patterns, which appear as dots in XRD^2 patterns [61, 62]. In addition to the dots corresponding to the (110) peaks of $Ti_3C_2T_x$, we also see the (109), (1012), (204), (205) peaks as shown by the blue arrows (left to right, respectively) in Figure 3r in the 5 wt% ML $Ti_3C_2T_x$-Al sample. These peaks can also be seen in $Ti_3C_2T_x$ clay as shown in Figure S14 by the blue arrows. The SEM images of the 5 wt% ML $Ti_3C_2T_x$-Al samples clearly shows the multi-layer particles of MXene on Al particles (Figure S13e, f). Based on our XRD^2 results, we have identified that we should expect to see the (110) peaks of single-to-few layer MXene in a bulk matrix and we should not expect to see the (00ℓ) peaks in low MXene concentrations.

After gaining understanding of $Ti_3C_2T_x$ XRD^2 pattern relation to the morphology of $Ti_3C_2T_x$ in the metal matrix, we next looked to understanding of the response of $Ti_3C_2T_x$ in Al through analysis of peak shifting during *in-situ* hot stage XRD^2 annealing. To roughly represent currently used densification temperatures of $Ti_3C_2T_x$ MXene in an Al matrix [40], we annealed our

room temperature compressed billet samples up to 550 °C on an AlN substrate in a domed *in-situ* hot stage in XRD and held at this temperature for 1 h in ambient conditions. In order to visualize more pronounced changes in the peak position of Al during *in-situ* annealing, we analyzed the shifting of the (311) peak of Al, as shown in Figure 4a (raw pattern is shown in Figure S15a). First, we utilized this peak shift to calculate the coefficient of thermal expansion (CTE) of Al in the pure Al and the $Ti_3C_2T_x$-Al composites, as shown in the green plot in Figure 4b. During this experiment, we noted that our Al control sample's CTE along the (311) plane in Al was $23.59 \pm 1.04 \times 10^{-6}$ K^{-1}, which is in agreeance with previous *in-situ* heated XRD studies on pure Al [63].

After establishing the baseline CTE for Al to ensure accuracy of our experiments, we next analyzed the difference in thermal strain of the Al (311) peak at 550 °C in the $Ti_3C_2T_x$/Al composites as compared to pure Al. Calculation of the strain using this method indicated that the single-to-few layer 2 wt% $Ti_3C_2T_x$ in Al caused a difference in thermal strain of -0.733 ± 0.546 $\mu\varepsilon$, which indicates a compressive strain is placed on the Al matrix by the reinforcing $Ti_3C_2T_x$ flakes. We expect the compressive strain on Al to be a result of the lower CTE of $Ti_3C_2T_x$ as compared to pure Al where $Ti_3C_2T_x$ will reduce expansion of the Al composite. In general, reduction of thermal expansion of metal matrices in composites indicates mechanical reinforcement of the matrix [64]. In order to ensure the compressive strain is due to reinforcement and not grain phenomena of Al, we analyzed the full-width at half maximum (FWHM) of the (311) peak of Al at 550 °C for 1 h (Figure S15b) and noted that the FWHM of the Al (311) peak was within 0.01 ° 2θ in all of the annealed composite samples. We next noted that 5 and 10 wt% inclusion of single-to-few layer $Ti_3C_2T_x$ and 5 wt% ML $Ti_3C_2T_x$ in the Al matrix results in a positive difference in thermal strain as compared to pure Al (up to 0.224 ± 0.546 $\mu\varepsilon$ for 5 wt% single-to-few layer $Ti_3C_2T_x$), which implies a tensile strain is applied on the Al matrix by the multi-

layer $Ti_3C_2T_x$ reinforcement. This could potentially be explained by the multi-layer nature of higher concentrations of $Ti_3C_2T_x$ flakes in Al. In previous atomic force microscopy (AFM) studies, $Ti_3C_2T_x$ multi-layer flakes have shown to have very low inter-layer adhesion, especially at increased temperatures, which could result in inter-flake shearing during thermal expansion of the Al matrix during annealing [27, 65]. This inter-flake shearing could cause application of a small tensile strain on Al, as shown by the purple plot in Figure 4b, as the inter-flakes of $Ti_3C_2T_x$ shear past each other and result in a positive difference in thermal strain for high loadings of $Ti_3C_2T_x$ due to the residual applied tensile strain in the structure. As this is the first identification of strain change in metal matrices due to stacking of MXenes, further in-situ studies are required to better understand this behavior.

After analysis of the residual strain in all the composites, we next used Vickers hardness testing to analyze the resultant mechanical properties of the billets after annealing at 550 °C for 1 h in the *in-situ* hot stage setup (Figure 4c) in air. To conduct the hardness testing, we took 5 to 6 indentations with a diamond pyramidal indenter using a load of 0.5 kg force on a polished surface of each billet, measured the diagonal dimensions to the nearest micron, calculated the Vickers microhardness of each indentation, and averaged the values to plot the bar graph with standard deviation (Figure 4c). For Al, the Vickers microhardness is 104.07 ± 8.31 HV, which agrees with previous studies on Al and Al composites using 0.5 kg force for Vickers testing [66-68]. For 1 and 2 wt% inclusion of single-to-few layer $Ti_3C_2T_x$ in Al, we see an increase up to 175.80 ± 8.32 HV for 2 wt% single-to-few flake $Ti_3C_2T_x$-Al. However, at 5 wt% single-to-few flake $Ti_3C_2T_x$-Al, we see a decrease to 120.30 ± 15.59 HV. This decrease could be due to similar reasons as previous graphene reinforced metal composites, where loosely bound flakes of multi-layer graphene result in stress concentrations within the matrix [69, 70]. However, we see a change in this established

trend for the Vickers values of 177.22 ± 12.15 HV and 208.36 ± 26.69 HV for 10 wt% single-to-few flake $Ti_3C_2T_x$-Al and 5 wt% multi-layer flake $Ti_3C_2T_x$-Al composites, respectively. We supposed that the difference in this trend as compared to established literature could be due to the stacking of $Ti_3C_2T_x$ flakes in Al, as noted by the presence of (00ℓ) peaks of $Ti_3C_2T_x$, so we focused on analysis of the evolution of the stacking of $Ti_3C_2T_x$ during annealing using *in-situ* XRD[2] methods.

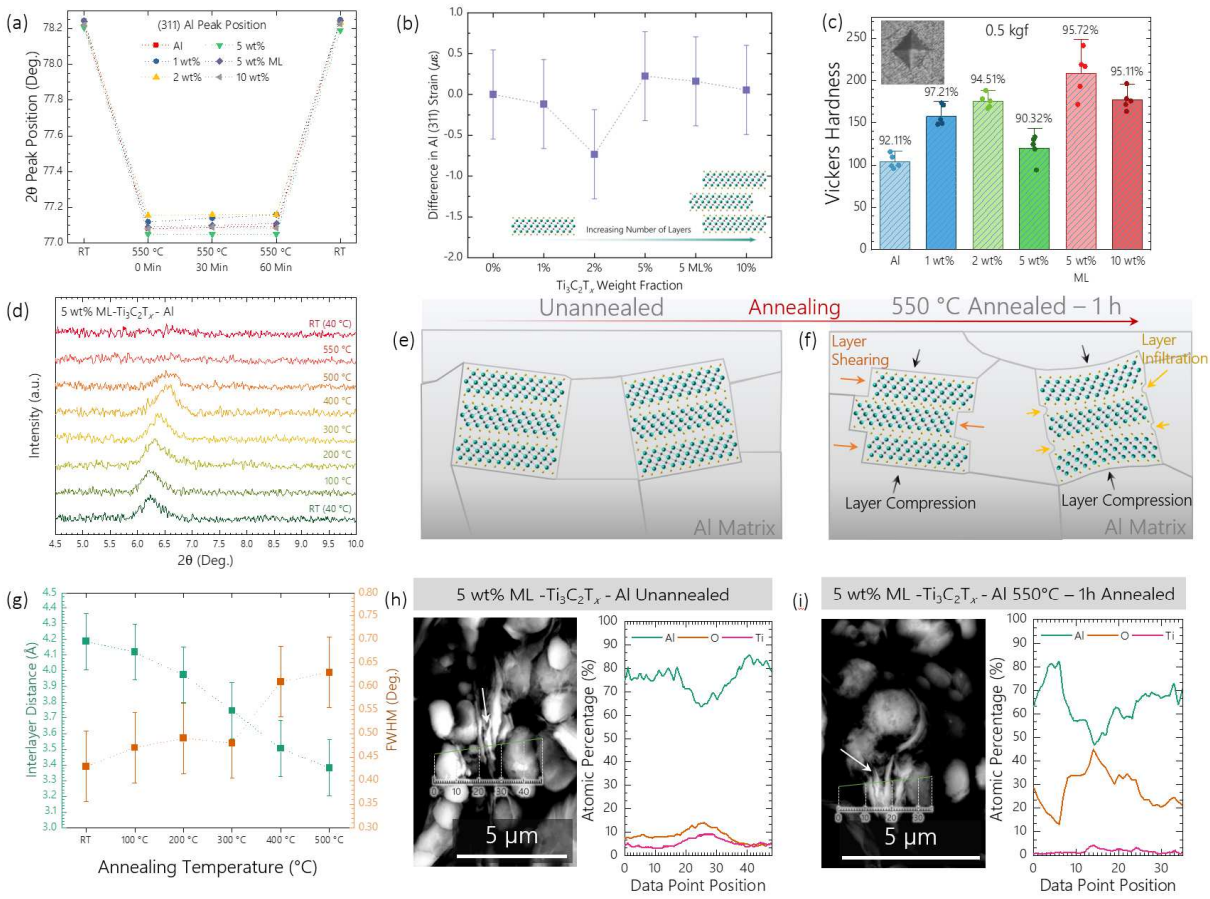

Figure 4. Thermal and mechanical behavior of $Ti_3C_2T_x$-Al composites annealed at 550 °C for 1 h. (a) The (311) peak shift of Al of all samples versus holding time at 550 ºC. (b) The shift of the (311) peak of Al illustrates residual strains in each annealed $Ti_3C_2T_x$/Al composite which is calculated by the difference in (311) Al peak positions compared to pure Al. (c) Vickers hardness of pure Al and all the $Ti_3C_2T_x$ -Al composites post-annealing. The error bars indicate the standard deviation and the numbers above the graph indicate relative densification. (d) *In-situ* XRD[2] of the (002) peak of $Ti_3C_2T_x$ from room temperature up to 550 °C indicates changes in the (002) peak

until it disappears at 550 °C. (e-f) Hypothesized mechanisms for loss of the (002) peak of $Ti_3C_2T_x$ during annealing are potential shearing or Al infiltration between the inter-layers of $Ti_3C_2T_x$. (g) Analysis of the (002) peak of $Ti_3C_2T_x$ during annealing. (h-i) SEM used in backscatter electron detection mode of the cross section of a fracture surface of the 5 wt% ML $Ti_3C_2T_x$-Al billets with EDS line-scans across the $Ti_3C_2T_x$ multi-layers. Arrows indicate multi-layers of $Ti_3C_2T_x$. Panel (h) is of non-annealed room-temperature compressed 5 wt% ML $Ti_3C_2T_x$-Al billet while panel (i) is of a 550 °C – 1 h annealed 5 wt% ML $Ti_3C_2T_x$-Al billet.

In order to understand how the (00ℓ) peaks of 10 wt% single-to-few flake and 5 wt% multi-layer flake $Ti_3C_2T_x$ in Al change during annealing, we again focused scans at 10° 2θ (0 to 25°) and scanned during *in-situ* XRD[2] annealing from room temperature (taken at 40 °C) up to 550 °C in ambient conditions at increments of 100 °C. The XRD spectra for 5 wt% multi-layer flake $Ti_3C_2T_x$ in Al are shown in Figure 4d. In both 10 wt% single-to-few flake and 5 wt% multi-layer flake $Ti_3C_2T_x$–Al, the (002) peak of $Ti_3C_2T_x$ slowly broadens and right-shifts until it is unintelligible from the signal noise. Only 5 wt% multi-layer flake $Ti_3C_2T_x$ in Al is discussed here as the peaks are more intense, likely due to its higher order of stacking as $Ti_3C_2T_x$ was not fully delaminated. The similar trend in (002) peak of $Ti_3C_2T_x$ in 10 wt% single-to-few flake $Ti_3C_2T_x$ during annealing is shown in Figure S16.

After visualizing the trend in the (002) peak changes during increasing annealing temperatures, we hypothesized that the loss of the (002) peak was due to changes in the morphology of the $Ti_3C_2T_x$ stacks of flakes, as previous literature did not see phase transformations of $Ti_3C_2T_x$ itself or $Ti_3C_2T_x$ in Al until 700 °C or beyond [39, 43]. All full spectrum diffractograms of pre- and post-annealed single-to-few flake and multi-layer flake $Ti_3C_2T_x$ in Al are shown overlaid in Figure S17. We surmised that the changes in morphology could be due to two mechanisms, as shown in Figure 4e-f. We speculated that the loss of (002) peaks in $Ti_3C_2T_x$ could be due to interlayer shearing of $Ti_3C_2T_x$ layers due to the compressive force placed on the stacks, as has been previously witnessed in AFM experiments [65], and/or due to partial Al infiltration in

between the stacks of $Ti_3C_2T_x$ layers during annealing, which has been suggested in previous studies of $Ti_3C_2T_x$ in Al using transmission electron microscopy methods [40]. Differential scanning calorimetry results shown in Figure S18 may indicate that interlayer shearing is more likely than Al interlayer infiltration, as Al infiltration would require lower melting temperatures of Al as the opening between the MXene layers (interflake spacing) is at the nano level, which is not seen in the Al melting point trends of mixed $Ti_3C_2T_x$-Al powders [71].

Another potential reason for shifting and loss of (002) peaks can be due to removal of intercalated species (such as water molecules), which might cause random ordering in stacked flakes. However, we do not believe this is the likely source of these (002) peak changes as previous studies show removal of intercalated species usually lead to a shift of the (002) peak to higher peak position accompanied by a decrease in FWHM, not the disappearance of the (002) peak as seen in this data [72, 73]. Regardless of the exact mechanism, the annealing of stacked $Ti_3C_2T_x$ in Al appears to alter the morphology of the $Ti_3C_2T_x$ stacks, as evidenced by the decreasing interlayer distance and increasing FWHM as evidenced by analysis of the (002) peak position and shape, as shown in Figure 4g. Future work should investigate this interfacial behavior of $Ti_3C_2T_x$ multilayer in Al composites, including the role of number of layers, surface groups, *etc*. However, this morphology alteration, which is different from pure $Ti_3C_2T_x$ behavior, appears to result in a change in the mechanical properties of the bulk composite, as the Vickers hardness values of the annealed 5 wt% ML $Ti_3C_2T_x$ in Al is 73% higher than that of 5 wt% single-to-few flake $Ti_3C_2T_x$ in Al.

After using *in-situ* XRD[2] methods to analyze the changes in the (002) peak of 5 wt% ML $Ti_3C_2T_x$ in Al, we next focused on using SEM and EDS line-scan methods to characterize the structure of the multi-layer $Ti_3C_2T_x$ both pre- and post-annealing. To prepare these samples for SEM and EDS analysis, we fractured the specimen and investigated the cross-sectional fracture

surface. In order to find the multi-layers of $Ti_3C_2T_x$, we used backscatter electron detection mode and identified brighter layered appearance of multi-layer $Ti_3C_2T_x$. We then used EDS line-scan analysis across the cross-section of the multi-layer $Ti_3C_2T_x$ (as marked by the white arrow). The signal attributed to the atomic percentage of Al decreases in accordance with an increase in signal attributed to the atomic percentage of Ti as the line-scan traverses across the cross-section of $Ti_3C_2T_x$ particles (Figure 4h). In addition, the increase in atomic percentage of O across the cross-section of multi-layer $Ti_3C_2T_x$ can be attributed to the O-containing surface groups of $Ti_3C_2T_x$. In contrast, the 5 wt% ML $Ti_3C_2T_x$-Al annealed at 550 °C – 1 h (Figure 4i) illustrates clear "fingers" which extend out of the stacked $Ti_3C_2T_x$ particles as marked by the white arrow (more images are shown in Figure S19). In the line scan, we note that the $Ti_3C_2T_x$ signal decreases while the Al signal increases as we reach the gaps between the "finger" extension of the multi-layer $Ti_3C_2T_x$ particle. In addition, the O atomic composition peaks at similar locations to that of Ti, which may indicate local oxidation at the interface between $Ti_3C_2T_x$ and Al, as seen in previous studies [40]. We do not believe the differences in EDS line scan compositions are due to surface roughness, as the multi-layer $Ti_3C_2T_x$ particle can be seen to be clearly exposed above the Al matrix in a secondary electron image as shown in Figure S20.

The trends in atomic composition across the "finger" like features in the backscatter electron SEM images in the annealed 5 wt% ML $Ti_3C_2T_x$-Al composite leads us to speculate that the loss of the (002) $Ti_3C_2T_x$ diffraction peak in both 5 wt% ML $Ti_3C_2T_x$ and 10 wt% single-to-few layer $Ti_3C_2T_x$ in Al may be due to morphological changes in the stacked $Ti_3C_2T_x$ during annealing of the composite mixture that we see in both pre-stacked multi-layer $Ti_3C_2T_x$ and re-stacked single-to-few layer $Ti_3C_2T_x$. It is possible that the increase in Vickers hardness for these specific composites could be due the increased available surface area between the $Ti_3C_2T_x$

"fingers" and Al for stress transfer, a potential increased ability to disrupt dislocation motion during plastic deformations in Al with these reaching "fingers" of $Ti_3C_2T_x$, or increased surface area for interfacial reaction of $Ti_3C_2T_x$-Al_2O_3-Al. I*n-situ* transmission electron microscopy studies of these deformed stacks of $Ti_3C_2T_x$ in Al are necessary to fully elucidate the strengthening mechanisms of these altered stacked layers of $Ti_3C_2T_x$. Future work will be needed to understand the reinforcement mechanisms of single-to-few and multi-layer flakes of $Ti_3C_2T_x$ in metal matrices and their relation to the structural, phase behavior, and oxidation stability of $Ti_3C_2T_x$ produced via different synthesis methods (molten salt, hydrofluoric acid) at the Al interface. Nevertheless, the increased reinforcement potential of multi-layer stacked $Ti_3C_2T_x$ particles at higher concentrations of $Ti_3C_2T_x$ in the Al matrix is an uncommon amongst other nanomaterials and could provide further evidence of the reinforcing capabilities MXene has for future metal matrix composites.

4. *Conclusion*

In this study, we have developed a self-assembly process of $Ti_3C_2T_x$ to aluminum which we can tune to create single-to-few layer dispersions of $Ti_3C_2T_x$ flakes from 1 to 5 wt%. In addition, we show that this same process can be used to include pre-stacked multi-layers of $Ti_3C_2T_x$ at 5 wt% or result in re-stacking of multi-layers of single-to-few flakes of $Ti_3C_2T_x$ at concentrations above 5 wt%. The ability to achieve near-full coverage of Al by $Ti_3C_2T_x$ can be used to create a network of $Ti_3C_2T_x$ in the Al matrix which can be used for multi-functional structural and/or conductive metal composites. This self-assembly process is also shown to be scalable to form large batches of $Ti_3C_2T_x$-Al powder, which makes this process advantageous for future additive manufacturing of bulk $Ti_3C_2T_x$-Al metal composites. Additionally, we have established XRD^2 as a powerful tool to detect small amounts of MXene in a bulk metal matrix as low as 1 wt%. Furthermore, the use of XRD^2 to detect single-to-few layer dispersions versus multi-layer

dispersions of MXene and analyze MXene's effects on the Al matrix as well as the morphological changes in MXene during annealing with *in-situ* methods will be helpful to further developments of bulk metal composites utilizing MXene for various applications. We believe this study serves to set the groundwork for future development of additively manufactured MXene-metal composites to continue to expand MXenes' wide array of promising applications.

Acknowledgments: We thank Office Naval Research (ONR) for partially funding this research under award number N00014-21-1-2799. We acknowledge the IUPUI OVCR funding. We are also thankful to Prof. Jian Xie for providing access to DSC.

[1] A.K.G. K. S. Novoselov, S. V. Morozov, D. Jiang, Y. Zhang, S. V. Dubonos, I. V. Grigorieva, A. A. Firsov, Electric Field Effect in Atomically Thin Carbon Films, Science 306 (2004).
[2] M. Naguib, M. Kurtoglu, V. Presser, J. Lu, J. Niu, M. Heon, L. Hultman, Y. Gogotsi, M.W. Barsoum, Two-dimensional nanocrystals produced by exfoliation of Ti_3AlC_2, Advanced Materials 23(37) (2011) 4248-53.
[3] M. Ghidiu, Lukatskaya, M.R., Zhao, M.Q., Gogotsi, Y., Barsoum, M.B., Conductive two-dimensional titanium carbide 'clay' with high volumetric capacitance, Nature 516 (2014) 78-81.
[4] D. Pinto, B. Anasori, H. Avireddy, C.E. Shuck, K. Hantanasirisakul, G. Deysher, J.R. Morante, W. Porzio, H.N. Alshareef, Y. Gogotsi, Synthesis and electrochemical properties of 2D molybdenum vanadium carbides – solid solution MXenes, Journal of Materials Chemistry A 8(18) (2020) 8957-8968.
[5] T. Mathis, Maleski, K., Goad, A., Sarycheva, A., Anayee, M., Foucher, A.C., Hantanasirisakul, K., Stach, E., Gogotsi, Y., Modified MAX Phase Synthesis for Environmentally Stable and Highly Conductive Ti_3C_2 MXene, ACS Nano 15 (2021) 6420-6429.
[6] Y. Li, H. Shao, Z. Lin, J. Lu, L. Liu, B. Duployer, P.O.A. Persson, P. Eklund, L. Hultman, M. Li, K. Chen, X.H. Zha, S. Du, P. Rozier, Z. Chai, E. Raymundo-Pinero, P.L. Taberna, P. Simon, Q. Huang, A general Lewis acidic etching route for preparing MXenes with enhanced electrochemical performance in non-aqueous electrolyte, Nature Materials 19(8) (2020) 894-899.
[7] V. Kamysbayev, Filatov, A.S., Hu, H., Rui, X., Lagunas, F., Wang, D., Klie, R.F., Talapin, D.V., Covalent surface modifications and superconductivity of two-dimensional metal carbide MXenes, Science 369(6506) (2020) 979-983.
[8] M. Li, J. Lu, K. Luo, Y. Li, K. Chang, K. Chen, J. Zhou, J. Rosen, L. Hultman, P. Eklund, P.O.A. Persson, S. Du, Z. Chai, Z. Huang, Q. Huang, Element Replacement Approach by Reaction with Lewis Acidic Molten Salts to Synthesize Nanolaminated MAX Phases and MXenes, Journal of the American Chemical Society 141(11) (2019) 4730-4737.
[9] M.A. Hope, A.C. Forse, K.J. Griffith, M.R. Lukatskaya, M. Ghidiu, Y. Gogotsi, C.P. Grey, NMR reveals the surface functionalisation of Ti_3C_2 MXene, Physical Chemistry Chemical Physics 18(7) (2016) 5099-102.
[10] Y. Gogotsi, B. Anasori, The Rise of MXenes, ACS Nano 13(8) (2019) 8491-8494.
[11] S.K. Nemani, B. Zhang, B.C. Wyatt, Z.D. Hood, S. Manna, R. Khaledialidusti, W. Hong, M.G. Sternberg, S.K.R.S. Sankaranarayanan, B. Anasori, High-Entropy 2D Carbide MXenes: $TiVNbMoC_3$ and $TiVCrMoC_3$, ACS Nano 15(8) (2021) 12815-12825.
[12] W. Hong, B.C. Wyatt, S.K. Nemani, B. Anasori, Double transition-metal MXenes: Atomistic design of two-dimensional carbides and nitrides, MRS Bulletin 45(10) (2020) 850-861.
[13] Z.W. Seh, K.D. Fredrickson, B. Anasori, J. Kibsgaard, A.L. Strickler, M.R. Lukatskaya, Y. Gogotsi, T.F. Jaramillo, A. Vojvodic, Two-Dimensional Molybdenum Carbide (MXene) as an Efficient Electrocatalyst for Hydrogen Evolution, ACS Energy Letters 1(3) (2016) 589-594.
[14] K.R.G. Lim, A.D. Handoko, S.K. Nemani, B. Wyatt, H.Y. Jiang, J. Tang, B. Anasori, Z.W. Seh, Rational Design of Two-Dimensional Transition Metal Carbide/Nitride (MXene) Hybrids and Nanocomposites for Catalytic Energy Storage and Conversion, ACS Nano 14(9) (2020) 10834-10864.
[15] M.R. Lukatskaya, S. Kota, Z. Lin, M.-Q. Zhao, N. Shpigel, M.D. Levi, J. Halim, P.-L. Taberna, M.W. Barsoum, P. Simon, Y. Gogotsi, Ultra-high-rate pseudocapacitive energy storage in two-dimensional transition metal carbides, Nature Energy 2(8) (2017).

[16] Y. Xia, T.S. Mathis, M.Q. Zhao, B. Anasori, A. Dang, Z. Zhou, H. Cho, Y. Gogotsi, S. Yang, Thickness-independent capacitance of vertically aligned liquid-crystalline MXenes, Nature 557(7705) (2018) 409-412.
[17] B. Anasori, M.R. Lukatskaya, Y. Gogotsi, 2D metal carbides and nitrides (MXenes) for energy storage, Nature Reviews Materials 2(2) (2017) 16098.
[18] J. Guo, B. Legum, B. Anasori, K. Wang, P. Lelyukh, Y. Gogotsi, C.A. Randall, Cold Sintered Ceramic Nanocomposites of 2D MXene and Zinc Oxide, Advanced Materials 30(32) (2018) 1801846.
[19] X. Xie, C. Chen, N. Zhang, Z.-R. Tang, J. Jiang, Y.-J. Xu, Microstructure and surface control of MXene films for water purification, Nature Sustainability 2(9) (2019) 856-862.
[20] Y.-H. Chen, M.-Y. Qi, Y.-H. Li, Z.-R. Tang, T. Wang, J. Gong, Y.-J. Xu, Activating two-dimensional $Ti_3C_2T_x$-MXene with single-atom cobalt for efficient CO_2 photoreduction, Cell Reports Physical Science 2(3) (2021).
[21] C.-F. Du, K.N. Dinh, Q. Liang, Y. Zheng, Y. Luo, J. Zhang, Q. Yan, Self-Assemble and In Situ Formation of $Ni_{1-x}Fe_xPS_3$ Nanomosaic-Decorated MXene Hybrids for Overall Water Splitting, Advanced Energy Materials 8(26) (2018).
[22] C.F. Du, X. Sun, H. Yu, Q. Liang, K.N. Dinh, Y. Zheng, Y. Luo, Z. Wang, Q. Yan, Synergy of Nb Doping and Surface Alloy Enhanced on Water-Alkali Electrocatalytic Hydrogen Generation Performance in Ti-Based MXene, Advanced Science 6(11) (2019) 1900116.
[23] A. Shayesteh Zeraati, S.A. Mirkhani, P. Sun, M. Naguib, P.V. Braun, U. Sundararaj, Improved synthesis of $Ti_3C_2T_x$ MXenes resulting in exceptional electrical conductivity, high synthesis yield, and enhanced capacitance, Nanoscale 13(6) (2021) 3572-3580.
[24] X. Zhang, Z. Zhang, Z. Zhou, MXene-based materials for electrochemical energy storage, Journal of Energy Chemistry 27(1) (2018) 73-85.
[25] J. Zhang, N. Kong, S. Uzun, A. Levitt, S. Seyedin, P.A. Lynch, S. Qin, M. Han, W. Yang, J. Liu, X. Wang, Y. Gogotsi, J.M. Razal, Scalable Manufacturing of Free-Standing, Strong $Ti_3C_2T_x$ MXene Films with Outstanding Conductivity, Advanced Materials (2020) 2001093.
[26] Y. Li, C. Wei, S. Huang, A. Ghasemi, W. Gao, C. Wu, V.N. Mochalin, In Situ Tensile Testing of Nanometer-Thick Two-Dimensional Transition-Metal Carbide Films: Implications for MXenes Acting as Nanoscale Reinforcement Agents, ACS Applied Nano Materials 4(5) (2021) 5058-5067.
[27] B.C. Wyatt, Rosenkranz, A., Anasori, B., 2D MXenes: Tunable Mechanical and Tribological Properties, Advanced Materials 33(6) (2021) 2007973.
[28] A. Lipatov, Lu, H., Alhabeb, M., Anasori, B., Gruverman, A., Gogotsi, Y., Sinitskii, A., Elastic properties of 2D $Ti_3C_2T_x$ MXene monolayers and bilayers, Science Advances 4(6) (2018) 1-7.
[29] A. Lipatov, M. Alhabeb, H. Lu, S. Zhao, M.J. Loes, N.S. Vorobeva, Y. Dall'Agnese, Y. Gao, A. Gruverman, Y. Gogotsi, A. Sinitskii, Electrical and Elastic Properties of Individual Single-Layer $Nb_4C_3T_x$ MXene Flakes, Advanced Electronic Materials 6 (2020).
[30] Y. Ul Haq, I. Murtaza, S. Mazhar, N. Ahmad, A.A. Qarni, Z. Ul Haq, S.A. Khan, M. Iqbal, Investigation of improved dielectric and thermal properties of ternary nanocomposite PMMA/MXene/ZnO fabricated by in-situ bulk polymerization, Journal of Applied Polymer Science 137(40) (2020).
[31] J. Lipton, G.-M. Weng, M. Alhabeb, K. Maleski, F. Antonio, J. Kong, Y. Gogotsi, A. Taylor, Mechanically Strong and Electrically Conductive Multilayer MXene Nanocomposites, Nanoscale 11 (2019) 20295-20300.

[32] Y.J. Mai, Y.G. Li, S.L. Li, L.Y. Zhang, C.S. Liu, X.H. Jie, Self-lubricating Ti_3C_2 nanosheets/copper composite coatings, Journal of Alloys and Compounds 770 (2019) 1-5.
[33] H. Zhang, L. Wang, Q. Chen, P. Li, A. Zhou, X. Cao, Q. Hu, Preparation, mechanical and anti-friction performance of MXene/polymer composites, Materials & Design 92 (2016) 682-689.
[34] J. Hu, S. Li, J. Zhang, Q. Chang, W. Yu, Y. Zhou, Mechanical properties and frictional resistance of Al composites reinforced with $Ti_3C_2T_x$ MXene, Chinese Chemical Letters 31(4) (2019).
[35] V. Kamysbayev, N.M. James, A.S. Filatov, V. Srivastava, B. Anasori, H.M. Jaeger, Y. Gogotsi, D.V. Talapin, Colloidal Gelation in Liquid Metals Enables Functional Nanocomposites of 2D Metal Carbides (MXenes) and Lightweight Metals, ACS Nano 13(11) (2019) 12415-12424.
[36] Y. Sliozberg, J. Andzelm, C.B. Hatter, B. Anasori, Y. Gogotsi, A. Hall, Interface binding and mechanical properties of MXene-epoxy nanocomposites, Composites Science and Technology 192 (2020).
[37] M. Fei, R. Lin, Y. Lu, X. Zhang, R. Bian, J. Cheng, P. Luo, C. Xu, D. Cai, MXene-reinforced alumina ceramic composites, Ceramics International 43(18) (2017) 17206-17210.
[38] H. Qing, D.U. Shi-Yu, D. Qi-Huang, C. Fan-Yan, S.I. Xiao-Yang, Preparation and Property of MXene/Copper Alloy Composites, Journal of Inorganic Materials 33(6) (2018).
[39] J. Zhang, S. Li, S. Hu, Y. Zhou, Chemical Stability of Ti_3C_2 MXene with Al in the Temperature Range 500-700 degrees °C, Materials 11(10) (2018).
[40] W. Zhou, Z. Zhou, Y. Fan, N. Nomura, Significant strengthening effect in few-layered MXene-reinforced Al matrix composites, Materials Research Letters 9(3) (2020) 148-154.
[41] M. Li, S. Wang, Q. Wang, F. Ren, Y. Wang, Preparation, microstructure and tensile properties of two dimensional MXene reinforced copper matrix composites, Materials Science and Engineering: A 803 (2021).
[42] B.C. Wyatt, S.K. Nemani, B. Anasori, 2D transition metal carbides (MXenes) in metal and ceramic matrix composites, Nano Convergence 8(1) (2021) 16.
[43] B.C. Wyatt, Nemani, S.K., Desai, K., Kaur, H., Zhang, B., Anasori, B., High-Temperature Stability and Phase Transformations of Titanium Carbide ($Ti_3C_2T_x$) MXene, Journal of Physics: Condensed Matter 33 (2021).
[44] D.R. Forrest, Jasiuk, I., Brown, L., Joyce, P., Mansour, A., Salamanca-Riba, L., Novel Metal-Matrix Composites with Integrally-Bound Nanoscale Carbon, Naval Surface Warfare Center, 2012.
[45] T. Knych, G. Kiesiewicz, P. Kwasniewski, A. Mamala, B. Smyrak, A. Kawecki, Fabrication and Cold Drawing of Copper Covetic Nanostructured Carbon Composites/ Otrzymywanie Oraz Ciągnienia Kompozytów Miedzianych Typu Covetic O Strukturze Nanometrycznej, Archives of Metallurgy and Materials 59(4) (2014) 1283-1286.
[46] M. Cao, D.B. Xiong, L. Yang, S. Li, Y. Xie, Q. Guo, Z. Li, H. Adams, J. Gu, T. Fan, X. Zhang, D. Zhang, Ultrahigh Electrical Conductivity of Graphene Embedded in Metals, Advanced Functional Materials 29(17) (2019).
[47] D. Lin, C. Richard Liu, G.J. Cheng, Single-layer graphene oxide reinforced metal matrix composites by laser sintering: Microstructure and mechanical property enhancement, Acta Materialia 80 (2014) 183-193.

[48] Z. Hu, F. Chen, D. Lin, Q. Nian, P. Parandoush, X. Zhu, Z. Shao, G.J. Cheng, Laser additive manufacturing bulk graphene-copper nanocomposites, Nanotechnology 28(44) (2017) 445705.
[49] M. Ghidiu, M.W. Barsoum, The {110} reflection in X-ray diffraction of MXene films: Misinterpretation and measurement via non-standard orientation, Journal of the American Ceramic Society 100(12) (2017) 5395-5399.
[50] K. Maleski, V.N. Mochalin, Y. Gogotsi, Dispersions of Two-Dimensional Titanium Carbide MXene in Organic Solvents, Chemistry of Materials 29(4) (2017) 1632-1640.
[51] Z. Ling, C.E. Ren, M.Q. Zhao, J. Yang, J.M. Giammarco, J. Qiu, M.W. Barsoum, Y. Gogotsi, Flexible and conductive MXene films and nanocomposites with high capacitance, Proceedings of the National Academy of Sciences of the United States of America 111(47) (2014) 16676-81.
[52] Q. Liu, M. He, X. Xu, L. Zhang, J. Yu, Self-assembly of graphene oxide on the surface of aluminum foil, New Journal of Chemistry 37(1) (2013) 181-187.
[53] Z. Li, G. Fan, Z. Tan, Q. Guo, D. Xiong, Y. Su, Z. Li, D. Zhang, Uniform dispersion of graphene oxide in aluminum powder by direct electrostatic adsorption for fabrication of graphene/aluminum composites, Nanotechnology 25(32) (2014) 325601.
[54] J. Evertsson, F. Bertram, F. Zhang, L. Rullik, L.R. Merte, M. Shipilin, M. Soldemo, S. Ahmadi, N. Vinogradov, F. Carlà, J. Weissenrieder, M. Göthelid, J. Pan, A. Mikkelsen, J.O. Nilsson, E. Lundgren, The thickness of native oxides on aluminum alloys and single crystals, Applied Surface Science 349 (2015) 826-832.
[55] U.P. Baoping Bob He, Kingsley L. Smith, Fundamentals of Two-Dimensonal X-Ray Diffraction (XRD2), Advances in X-ray Analysis 43 (2000).
[56] B. He, Two-dimensional X-ray Diffraction, John Wiley & Sons, Inc.2018.
[57] C.E. Ren, K.B. Hatzell, M. Alhabeb, Z. Ling, K.A. Mahmoud, Y. Gogotsi, Charge- and Size-Selective Ion Sieving Through $Ti_3C_2T_x$ MXene Membranes, The Journal of Physical Chemistry Letters 6(20) (2015) 4026-4031.
[58] M. Han, C.E. Shuck, R. Rakhmanov, D. Parchment, B. Anasori, C.M. Koo, G. Friedman, Y. Gogotsi, Beyond $Ti_3C_2T_x$: MXenes for Electromagnetic Interference Shielding, ACS Nano 14(4) (2020) 5008-5016.
[59] T. Yun, H. Kim, A. Iqbal, Y.S. Cho, G.S. Lee, M.K. Kim, S.J. Kim, D. Kim, Y. Gogotsi, S.O. Kim, C.M. Koo, Electromagnetic Shielding of Monolayer MXene Assemblies, Advanced Materials (2020) 1906769.
[60] Y. Dong, S. Chertopalov, K. Maleski, B. Anasori, L. Hu, S. Bhattacharya, A.M. Rao, Y. Gogotsi, V.N. Mochalin, R. Podila, Saturable Absorption in 2D Ti3 C2 MXene Thin Films for Passive Photonic Diodes, Advanced Materials 30(10) (2018).
[61] E. Bontempi, D. Benedetti, A. Zacco, E. Pantos, S. Boniotti, C. Saletti, P. Apostoli, L.E. Depero, Analysis of crystalline phases in airborne particulate matter by two-dimensional X-ray diffraction (XRD^2), Journal of Environmental Monitoring 10(1) (2008) 82-8.
[62] A.B. Rodriguez-Navarro, XRD 2DScan: new software for polycrystalline materials characterization using two-dimensional X-ray diffraction, Journal of Applied Crystallography 39(6) (2006) 905-909.
[63] G. Langelaan, S. Saimoto, Thermal expansion measurement of pure aluminum using a very low thermal expansion heating stage for x-ray diffraction experiments, Review of Scientific Instruments 70(8) (1999) 3413-3417.

[64] S.E. Shin, Y.J. Ko, D.H. Bae, Mechanical and thermal properties of nanocarbon-reinforced aluminum matrix composites at elevated temperatures, Composites Part B: Engineering 106 (2016) 66-73.
[65] X. Zhou, Y. Guo, D. Wang, Q. Xu, Nano friction and adhesion properties on Ti_3C_2 and Nb_2C MXene studied by AFM, Tribology International 153 (2020) 106646.
[66] M. Dhanashekar, P. Loganathan, S. Ayyanar, S.R. Mohan, T. Sathish, Mechanical and wear behaviour of AA6061/SiC composites fabricated by powder metallurgy method, Materials Today: Proceedings 21 (2020) 1008-1012.
[67] B. Siddharthan, R. Rajiev, S. Saravanan, T.K. Naveen, Effect of Silicon Carbide in Mechanical Properties of Aluminium Alloy Based Metal Matrix Composites, in: IOP (Ed.) IOP Conference Series: Materials Science and Engineering, IOP, 2020, p. 764.
[68] K. Kaviyarasan, S. Thiyagu, V. Shabari, R. Saileswaran, S. Siva sankaran, T. Sivanesan, Investigation on mechanical properties of aluminium alloy A356 by reinforcing with TiB_2 & WC composites, in: IOP (Ed.) IOP Conf. Series: Materials Science and Engineering, IOP, 2021, p. 1145.
[69] S.E. Shin, H.J. Choi, J.H. Shin, D.H. Bae, Strengthening behavior of few-layered graphene/aluminum composites, Carbon 82 (2015) 143-151.
[70] W. Zhou, Y. Fan, X. Feng, K. Kikuchi, N. Nomura, A. Kawasaki, Creation of individual few-layer graphene incorporated in an aluminum matrix, Composites Part A: Applied Science and Manufacturing 112 (2018) 168-177.
[71] Shahram Amini, J.M.C. Gallego, L. Daemen, A.R. McGhie, C. Ni, L. Hultman, M. Ode´n, M.W. Barsoum, On the Stability of Mg Nanograins to Coarsening after Repeated Melting, Nano Letters 9 (2009) 3082-3086.
[72] A. Iqbal, F. Shahzad, K. Hantanasirisakul, M.K. Kim, J. Kwon, J. Hong, H. Kim, Y. Gogotsi, C.M. Koo, Anomalous absorption of electromagnetic waves by 2D transition metal carbonitride Ti_3CNT_x (MXene), Science 369 (2020) 446-450.
[73] K.D. Fredrickson, B. Anasori, Z.W. Seh, Y. Gogotsi, A. Vojvodic, Effects of Applied Potential and Water Intercalation on the Surface Chemistry of Ti_2C and Mo_2C MXenes, The Journal of Physical Chemistry C 120(50) (2016) 28432-28440.

Self assembly of $Ti_3C_2T_x$ onto Al flakes

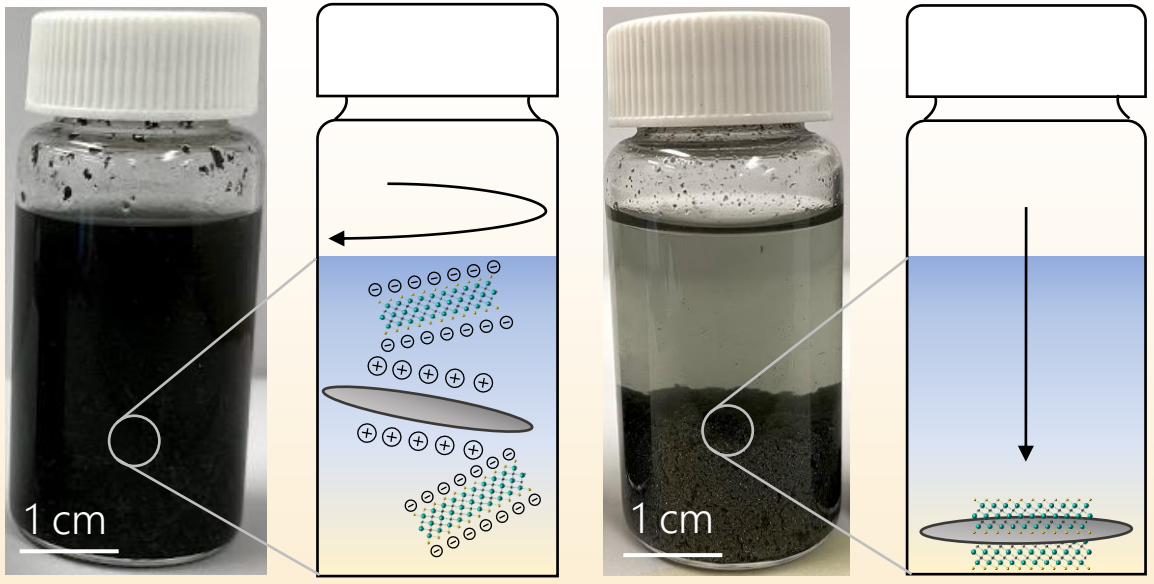

Solution mixing of delaminated $Ti_3C_2T_x$ + Al → Self-assembled single-to-few layer $Ti_3C_2T_x$ + Al powder

In-situ hot stage XRD[2]